Identifying the Source of Ultraviolet Emission Powering He II Lines in Metal-Poor Dwarf Galaxies

ialtunin@unr.edu

Ivan Altunin[1], C Ellis[1], R Tanner[1], R Plotkin[1], C White[1], R Soria[2], A Reines[3], M Pakull[4], E Gallo[5], R Urquhart[6]

1. University of Nevada, Reno Physics Department, 2. INAF, Osservatorio Astrofisico di Torino, Strada Osservatorio, 3. Montana State University, 4. Observatoire Astronomique de Strasbourg, 5. University of Michigan, 6. Michigan State University

1. Introduction

Big Picture Goal: We seek to use stellar population synthesis modeling to resolve the star formation histories of metal-poor star-forming galaxies, in conjunction with multi-wavelength X-ray observations, to investigate the plausibility of accreting compact objects within these galaxies (both present and in the near-past), being the primary sources of He II ionization.

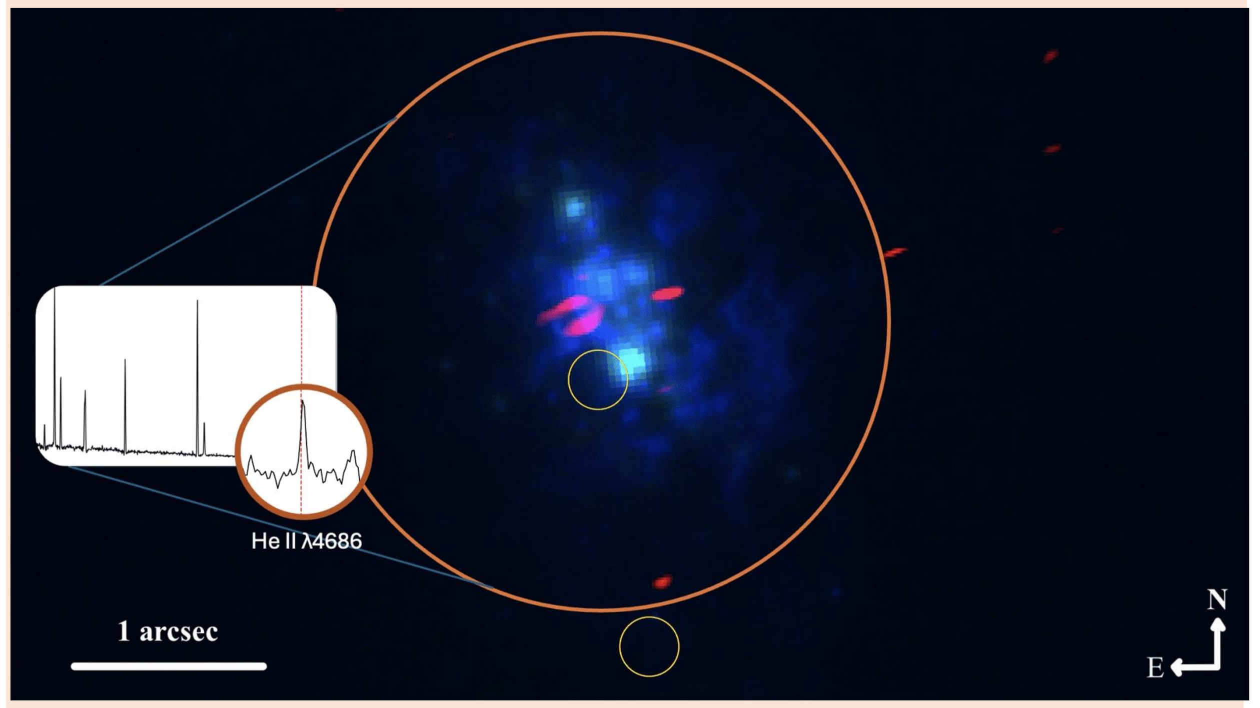

Figure 1: RGB composite image of HST (from Thygesen et al. 2023) and VLA X-band (8-12 GHz) of one Blue Dwarf Galaxy Mrk1434, in our 23 galaxy sample. The X-band is pictured in red, near-infrared in green, and the optical in blue. The yellow circles picture the locations of the two ULXs with positional uncertainties of 0.31". The orange circle represents the size of the SDSS fiber whose spectrum was analyzed in this work.

Statement of the Problem

1.1 Star-Formation Woes: Recent observations from JWST challenge existing models of galaxy formation by revealing unexpectedly high star formation rates and surprisingly mature and complex structures in distant galaxies (Xiao et al., 2024).

1.2 Early Universe Analogs: Metal-poor, star-forming blue dwarf galaxies serve as critical analogs for understanding how early-universe galaxies evolved (e.g., Mezcua 2019).

1.3 Spectral Anomalies: A subset of such metal-poor blue dwarf galaxies exhibit strong HeII λ4686 emission lines (Figure 1), which requires the presence of a substantial ultraviolet (EUV) continuum with energy between 54 to 300 eV; Kehrig et al. 2018; Ponnada et al. 2020)

Question: What is powering this EUV-induced He II line?

Helium Ionization Mechanisms

1.4 Wolf-Rayet Stars: Wolf-Rayet (WR) stars, where strong winds from massive stars expose hotter regions closer to the stellar core, provide a natural and sufficient source of EUV photons (Schaerer 1996).

1.4.1 Uncommon at Lower Metallicity

1.5 Accreting Compact Objects: Accreting compact objects, such as X-ray binaries (XRBs) and/or active galactic nuclei (AGN), can also provide significant EUV radiation due to their accretion processes (Shirazi and Brinchman, 2012)

1.5.1 Excess of luminous XRBs: Observational studies show an empirical relationship between luminous XRBs in metal-poor galaxies with high star formation rates (Brorby et al. 2014; Lehmer et al. 2021) of the form:

$$\log\left(\frac{L_X}{\mathrm{ergs}^{-1}}\right) = a\log\left(\frac{\mathrm{SFR}}{\mathrm{M_\odot yr^{-1}}}\right) + b\log\left(\frac{\mathrm{(O/H)}}{\mathrm{(O/H)_\odot}}\right) + c,$$

1.6 Modeling Galaxy Evolution: The above relationships often assume the current SFR to be averaged over the last 10 or 100 Myr. As a result, they offer an incomplete understanding without considering how the star formation rate changes with time - the star formation history (SFH) of a galaxy - which can be modeled to a high temporal-resolution using Stellar Population Synthesis (SPS) methods (Leja et al., 2019).

2. Data

2.1 Sample Selection: We perform a Chandra X-ray survey of 23 (Figure 2) nearby (z < 0.1) star-forming galaxies that show nebular He II emission but lack the spectral signatures of Wolf-Rayet stars originally identified by Shirazi & Brinchmann (2012).

2.2 X-Ray Data: Chandra X-Ray observations were obtained for 7 new galaxies and 16 archival galaxies (Evans et al. 2024). The high spatial resolution and sensitivity of Chandra allow us to locate any detected X-ray sources within each host galaxy, to then investigate if they are emitting sufficient EUV photons in the *present* time to power the observed He II line (Section 5.3).

2.3 Spectral and Photometric Data: SDSS Photometry and Spectra were obtained for 12 of our 23 galaxies with data over a suitable SNR threshold of 10 (York et al. 2000). This data was used to model the stellar populations and SFH (Section 3.2)

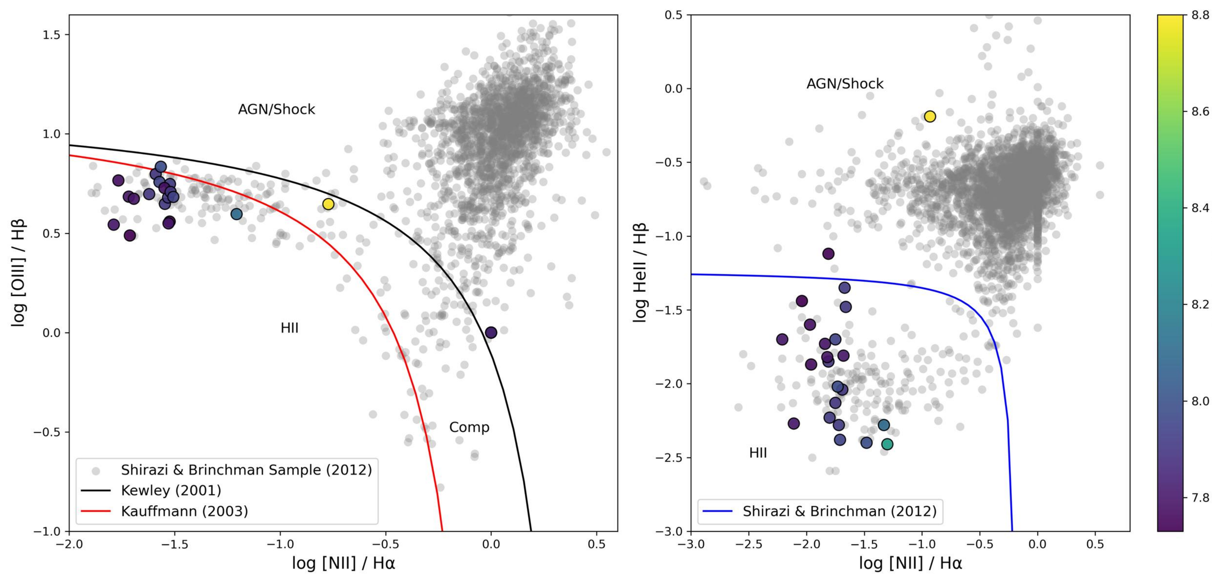

Figure 2: Line ratios plotted for the parent sample of galaxies (grey points) from Shirazi and Brinchman (2012), with the colored points representing our sub-sample of 23 nearby star-forming galaxies that show nebular He II emission but lacking Wolf-Rayet star signatures, each color-coded by the measured solar metallicity. The boundaries defined by the Kauffmann (2003) and Kewley (2001) lines divide the diagram into different regions, which are used, in conjunction with the Shirazi and Brinchman empirical relationship, to classify the galaxies.

4. Stellar Population Analysis

4.1 Stellar Population Modeling: We model the stellar population for the 12 galaxies in our sub-sample by simultaneously fitting their photometry and spectra using Stellar Population Synthesis (SPS) (Figure 3). SPS simulates the light generated from a population of stars of a certain metallicity and convolves their stellar evolution with the rate of new stars born at a given time - over the entire SFH of the galaxy.

3.4 Tools: We used Prospector (Johnson, 2021), which uses a Bayesian approach to fit the spectra, adopting empirically derived MIST Isochrone (Dotter, 2016) and MILES Spectral stellar libraries (Sanchez-Blazquez, 2006)

4.2 Star Formation Rates: It is apparent that the galaxies within our sample with X-ray detections are emitting as much, or more, X-rays as expected by the empirical relations described in Sec 1..1 (Figure 4).

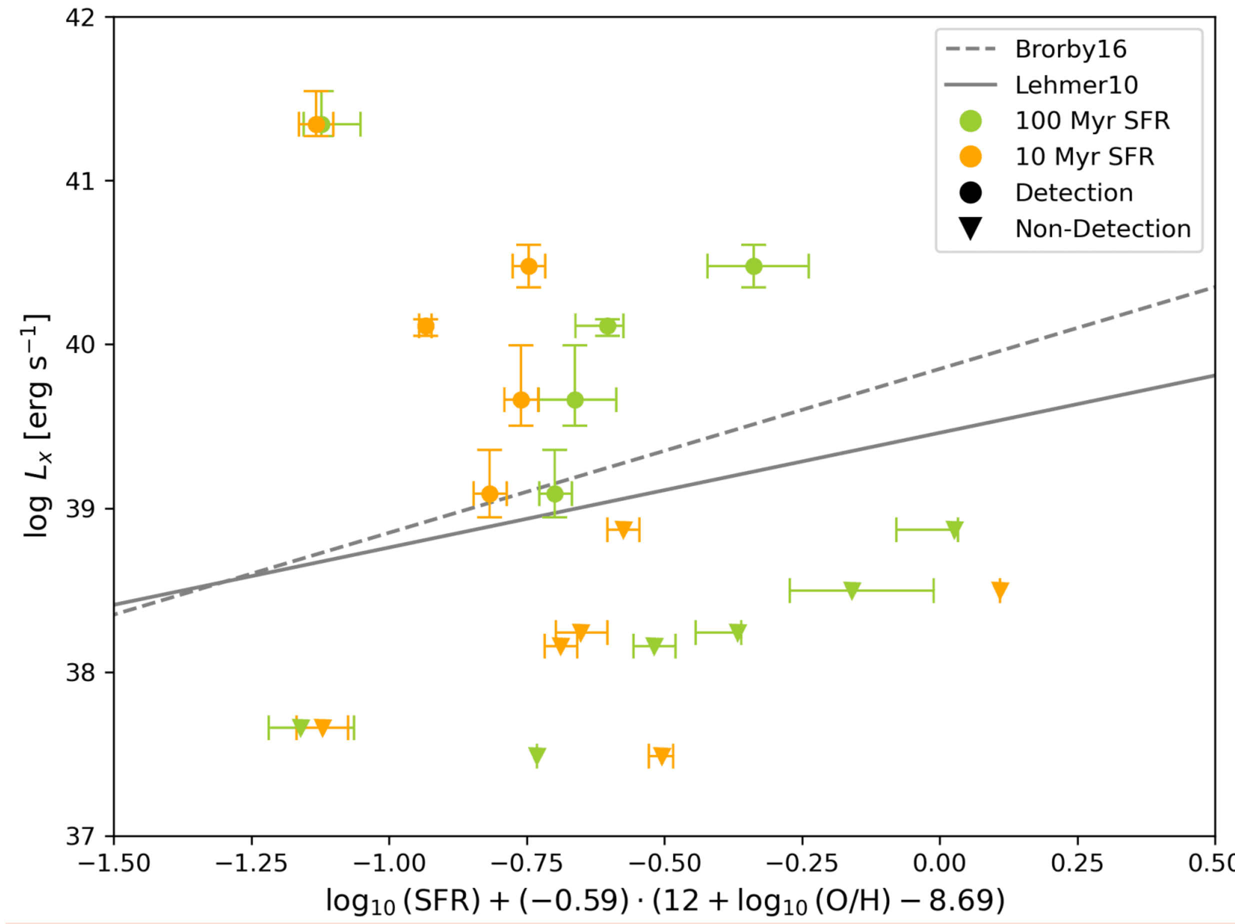

Figure 4: X-ray luminosity-SFR-metallicity relationship plotted with reference lines from Lehmer (2010) and Brorby (2016). Upper limits are plotted as triangles for non detections. SFR taken as the value of the last SFH bin modeled for epochs of 100 Myr and 10 Myr (Figure 3).

3. Data Analysis

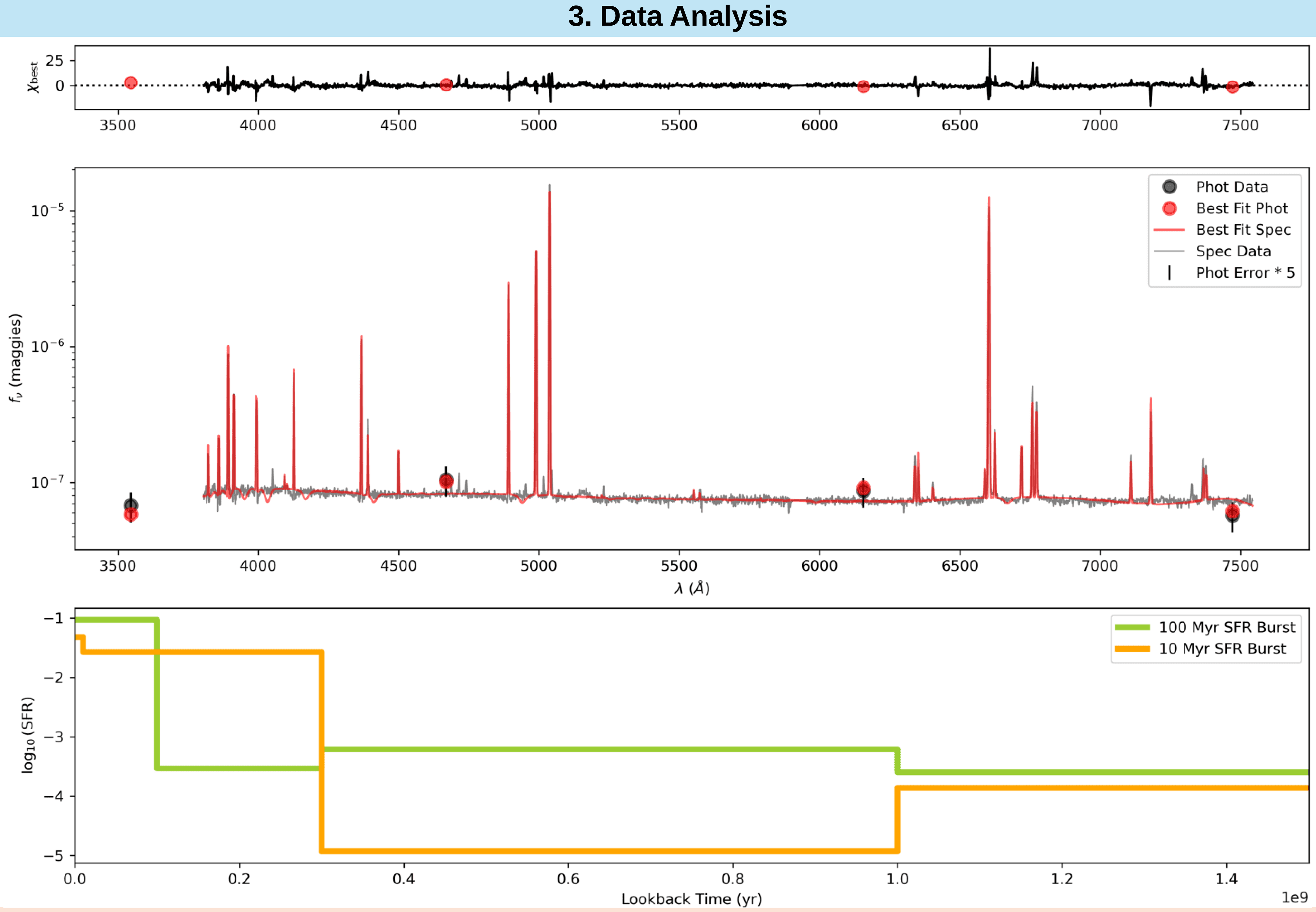

Figure 3: Example simultaneous spectra/photometric fit (middle) with residuals (top), and the resulting star formation history (bottom) for two cases - final burst lasting (1) 100 Myr and (2) 10 Myr

5 X-Ray Data Analysis

5.1 X-ray Reduction: All X-ray observations, archival and new, were reduced using Chandra Interactive Analysis of Observations (CIAO) (Fruscione et al. 2006).

5.1.1 X-ray Spectral Fitting: X-ray spectra were extracted and, we estimated unabsorbed fluxes with a power-law model (Γ = 1.7) and diskbb model (kT = 1.2 keV)

5.2 Modeled EUV Continuum: We extrapolated each spectral fit to 0.054-0.3 keV to estimate an unabsorbed EUV photon flux density for each galaxy (Figure 5).

5.3 X-Ray Brightness: Despite being bright in the X-ray due to accreting bodies (Figure 4), there is still a deficit of sufficient EUV ionizing photons to power the He II line for the majority of our sample (Figure 5).

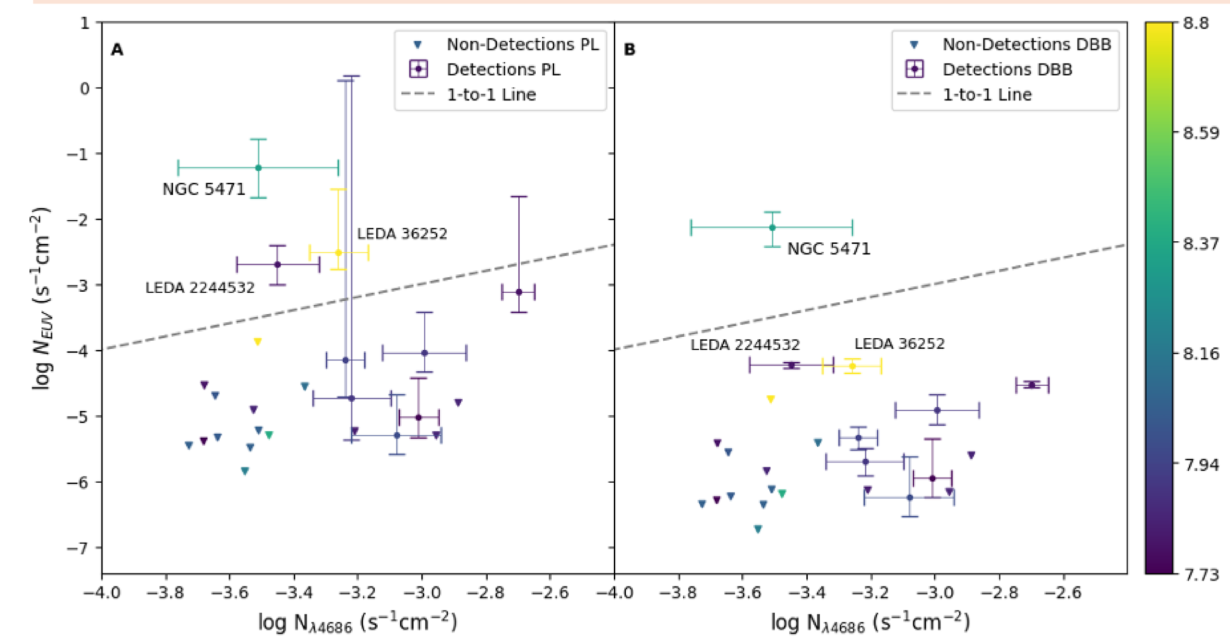

Figure 5: Unabsorbed EUV photon flux estimated to be produced from accreting X-ray objects is compared to required EUV photon flux to produce the observed HeII λ4686 line. Panel A illustrates power-law modeling and panel B demonstrates diskbb modeling (Section 3.1.1). Almost all detections show a deficit in EUV photon flux to account for the observed HeII emission line strength, as evident by most data points falling under the 1-to-1 line.

6 Conclusions

6.1.1: Current He II ionization explanations are limited to the processes happening at the current time.

6.1.2: Current stellar population (including lack of Wolf-Rayet stars) is an implausible cause for He II ionization.

6.1.3: Current X-ray sources are suitably bright for the measured SFR and metallicity but are still an implausible cause for HeII ionization.

6.2: Advanced SPS modeling may help recover this missing information by studying SFHs that may have had more chaotic large bursts of star formation than previously expected.

References/Acknowledgments

The scientific results reported in this article are based in part on observations made by the Chandra X-ray Observatory and data obtained from the Chandra Data Archive. This research has made use of software provided by the Chandra X-ray Center (CXC) in the application packages CIAO.

This work was supported by NASA NVSGC under award No. 80NSSC20M0043.

Abazajian, K. N. et al., 2009. doi:10.1088/0067-0049/182/2/543.
Brorby, M., Kaaret, P., and Prestwich, A., 2014. doi:10.1093/mnras/stu736.
Dotter, A., 2016. doi:10.3847/0067-0049/222/1/8.
Elmegreen, D. M. et al., 2016. doi:10.3847/0004-637X/825/2/145.
Evans, I.N., et al. 2024, doi:10.3847/1538-4365/ad6319
Garofali, K., et al. 2024. doi:10.3847/1538-4357/ad0a6a.
Gelbord, J. M., Mullaney, J. R., and Ward M. J., 2009. doi:10.1111/j.1365-2966.2009.14961.x.
Houck, J. C., and DeNicola, L. A., 2000.
Johnson, B. D., Leja, J., Conroy, C., and Speagle, J. S.,, 2021. doi:10.3847/1538-4365/abef67
Kauffmann, G. et al, 2003. doi:10.1111/j.1365-2966.2003.07154.x.
Kehrig, C., 2018. doi:10.1093/mnras/sty1920.
Kewley, L. et al., 2001. doi:10.1086/321545.
Leja, J., Johnson, B. D., Conroy, C., van Dokkum, P. G., and Byler, N., 2017. doi:10.3847/1538-4357/aa5ffe.
Mezcua, M, 2019. doi:10.1038/s41550-018-0662-2.
Ponnada, S., Brorby, M., and Kaaret, P., 2020. doi:10.1093/mnras/stz2929.
Sánchez-Blázquez, P. et al., 2006. doi:10.1111/j.1365-2966.2006.10699.x.
Shirazi, M. and Brinchmann, 2012. doi:10.1111/j.1365-2966.2012.20439.x.
Sun, W. et al, 2012. doi:10.1088/0004-637X/760/1/61.
Thygesen, E., 2023. doi:10.1093/mnras/stad002.
Xiao, M., 2024. doi:10.1038/s41586-024-08094-5.
York, D. G. et al., 2000. doi:10.1086/301513.